JTTEE5 16:245–260
DOI: 10.1007/s11666-007-9023-x
1059-9630/$19.00 © ASM International

Three Dimensional Modeling of the Plasma Spray Process

He-Ping Li and E. Pfender

(Submitted October 31, 2005; in revised form January 15, 2006)

Results of simulations of three-dimensional (3D) temperature and flow fields inside and outside of a DC arc plasma torch in steady state are presented with transverse particle and carrier gas injection into the plasma jet. The results show that an increase of the gas flow rate at constant current moves the anode arc root further downstream leading to higher enthalpy and velocity at the exit of the torch anode, and stronger mixing effects in the jet region. An increase of the arc current with constant gas flow rate shortens the arc, but increases the enthalpy and velocity at the exit of the torch nozzle, and leads to longer jets. 3D features of the plasma jet due to the 3D starting conditions at the torch exit and, in particular, due to the transverse carrier gas and particle injection, as well as 3D trajectories and heating histories of sprayed particles are also discussed.

Keywords plasma spray, three-dimensional modeling, particle behavior

1. Introduction

Over the past few decades, thermal plasma spraying has been widely employed in various industries for preparing different kinds of coatings, such as wear-, corrosion- or oxidation-resistant coatings, thermal barrier coatings, etc. (Ref 1). A schematic diagram of an atmospheric-pressure thermal plasma spray system is shown in Fig. 1. In this system, the plasma working gas flows through the small space between cathode and anode, where the gas is heated and partially ionized forming an arc plasma. The high-temperature plasma jet, emanating from the anode nozzle, will heat and accelerate particles, injected into the high-temperature gas region by means of a cold carrier gas perpendicular to the axis of the plasma jet. The heated powders inside the jet region will impact and adhere to the substrate forming a coating.

Numerous factors may affect the spray efficiency and coating quality, including the plasma torch geometry and operating parameters, carrier gas flow rate and injection location, particle size and its distributions, materials, injection velocity and direction, substrate (or work-piece) location, temperature and surface conditions, etc. Since optimization of the spray process parameters using a purely empirical approach is a rather time-consuming task, numerical simulation has been accepted as a useful and economical tool to understand the effects of various parameters on the coating quality, and thus, on optimization the plasma spray process.

Because of the complex interactions between electromagnetic fields, the plasma flow and temperature fields, the heat and flow patterns inside the plasma torch will always be unsteady and three-dimensional (3D). Over the past few decades, many papers concerning numerical (Ref 2-8) and experimental (Ref 9) studies of the characteristics of DC arc plasma torches have been published. Although the previous two-dimensional (2D) modeling method (Ref 2-8) can, to some extent, predict the heat transfer and flow patterns inside the plasma torch correctly, the predicted arc voltage of the torch in the turbulent regime is much higher (two- or three-fold) than the measured value, and the predicted axial location of the arc attachment at the anode surface is also much farther downstream than that observed in experiments (Ref 10, 11), due to the significant local attachment of the anode arc-root on the anode inner surface. The incrustation pattern at the outer surface of the torch anode, as shown in Fig. 2, indicates that the arc root in the torch always attaches in the shape of a more or less constricted spot at the anode inner surface (Ref 12). In recent years, with the fast development of computer hardware and software, 3D modeling of heat transfer and fluid flow for arc plasmas has become feasible (Ref 13-18), even for the thermal plasma torch with axisymmetrical geometries (Ref 12, 19-22). As indicated by Wutzke (Ref 9), there are three different arc operation modes for non-transferred DC arc plasmas, i.e., a steady mode, a restrike mode and a takeover mode accompanied by the corresponding ''symptomatic behavior'' of the arc. For a steady mode of operation, the Steenbeck's minimum principle (Ref 23) is employed to determine the axial position of the anode arc-root at the anode surface (Ref 21, 22). The modeling results indicate that the temperature and flow fields inside the DC non-transferred arc plasma

He-Ping Li, Department of Engineering Physics, Tsinghua University, Beijing, 100084, P.R. China; Contact e-mail: liheping@tsinghua.edu.cn. **E. Pfender,** Department of Mechanical Engineering, University of Minnesota, Minneapolis, MN, 55455.

Nomenclature

$\vec{B}$	self-induced magnetic induction intensity vector
c_1, c_2, c_μ, σ_K, σ_ε	turbulent model constants
c_p	specific heat at constant pressure
D_p	particle diameter
$\bar{D}_p$	averaged diameter of particles
e	elementary charge
F_r, F_θ, F_z	components of Lorentz force in r-, θ-, and z-directions
$\vec{F}$	Lorentz force vector
G	turbulent generation term
j_r, j_θ, j_z	components of the current density vector in r-, θ-, and z-directions
$\vec{j}$	electric current density vector
K	turbulent kinetic energy
k	thermal conductivity
k_B	Boltzmann constant
L_{jet}	length of the high temperature region
N_p	sampling particle number
Pr_t	turbulent Prandtl number
p	gas pressure
$Q_{current}$	energy source term related to the current
r	coordinate in r-direction
$\bar{r}_p$	averaged radial position of particles
S_R	radiation loss per unit volume of the plasma
T	gas temperature
T_p	particle temperature
$\bar{T}_p$	averaged temperature of particles
$\vec{v}$	velocity vector
v_r, v_θ, v_z	velocity components in r-, θ-, and z-directions
V_{in}	velocity of the carrier gas
x_p	x-position of particles
$\bar{x}_p$	averaged x-position of particles
y_p	y-position of particles
$\bar{y}_p$	averaged y-position of particles
z	coordinate in z-direction

Greek Letters

Δα	deflection angles of the plasma jet from its referenced characteristic axis
Γ	effective 'diffusion' coefficient
α	deflection angle of the jet
ε	turbulent kinetic energy dissipation rate
ϕ	electric potential
μ	molecular viscosity
μ_t	turbulent viscosity
θ	coordinate in θ -direction
ρ	mass density
σ	electric conductivity
σ_D	characteristic diameter range of particle dispersions
σ_p	characteristic pattern radius of particle dispersions
σ_T	characteristic temperature range of particle dispersions

Subscript Letters

D	diameter
p	particle or position
r	radial direction
T	temperature
t	turbulence
z	axial direction
θ	circumferential direction

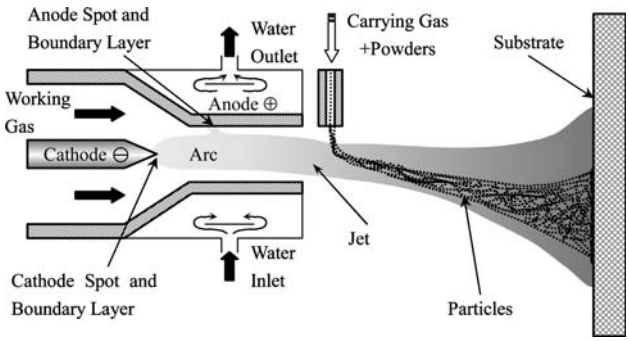

Fig. 1 Schematic diagram of thermal plasma spraying system

Fig. 2 Incrustation pattern at the outer surface of the arc anode (Ref 12)

torch show significant 3D features. When the plasma torch works in a restrike mode or takeover mode, the anode arc-root moves along the anode inner surface with time, and the heat transfer and flow patterns will be of time-dependence. This unsteady phenomenon would result in instabilities in the plasma jet region, and also be enhanced by the turbulent mixing with the ambient gas when the plasma jet issues into the quiescent surrounding gas.

Recently, Vardelle and her coworkers (Ref 24, 25) conducted 3D, transient modeling on the heat transfer and fluid flow inside a non-transferred DC arc plasma torch for a restrike mode of operation.

The 3D heat transfer and flow patterns, as well as the ionization-recombination process, inside a thermal plasma torch also have significant effects on the characteristics of the thermal plasma jet issuing from the exit of the plasma torch and, for example, on the quality of the coatings obtained by plasma spray. Over the past few decades, many papers have been devoted to modeling of the DC arc plasma spray process or to the study of spray-related basic processes based on 2D (axi-symmetrical) assumption with neglecting the effects of the transverse injection of the cold carrier gas on the jet flow field and on particle behavior (Ref 4, 26-43). But experimental results showed that even a small amount of carrier gas (5% of the main flow) transverse injection, as well as the particles used as the tracers in LDV measurements, may induce a deflection of the plasma jet with a deflection angle as great as 5°, and this 3D effect must be taken into account in the interpretation of the LDV data (Ref 35). In Recent years, 3D modeling work concerning the effects of transverse gas injection from a single injection port on the plasma jet characteristics and the trajectories of injected particles attracted increasing interest (Ref 44-52). The common feature of most of these papers is that assumed 2D temperature and velocity distributions at the outlet of the torch nozzle (or the inlet of the plasma jet region) are employed as boundary conditions for 3D modeling of heat transfer, flow patterns, and particle behavior in the jet region, i.e., only the effect of the carrier gas injection on the 3D characteristics of the plasma jet is included in the modeling work (Ref 26-43). Using velocity and temperature profiles obtained from modeling of DC arc plasma torches as the starting conditions of plasma jets (Ref 4, 53) depends strongly on the ability to model plasma torches. Based on the 3D modeling of thermal plasma torches (Ref 19-22), it is known that the temperature and velocity distributions at the exit of the plasma torches are non-axi-symmetric, which is expected to influence the temperature and flow fields within the plasma jet region.

In the present paper, more realistic 3D temperature and flow fields inside and outside of a DC arc plasma torch are predicted with transverse particle and carrier gas injection into the plasma jet. In this study, the calculation domain is divided into two sub-domains, i.e., the torch region and the plasma jet region. And the calculated temperature and flow fields at the exit of the plasma torch are used as the starting boundary conditions for modeling of the plasma jet region. Thus, the 3D features due to both the 3D profiles at the exit of the plasma torch and the transverse injection of the cold carrier gas can be investigated. Based on the computed plasma temperature and flow fields, the particle 3D trajectories and heating histories are predicted. In this paper, the effect of particle injection on the flow field is neglected assuming a low-particle loading rate.

2. Modeling Approach: Flow and Temperature Fields

2.1 Basic Assumptions

In this paper, the following basic assumptions are employed for simulating the heat transfer and flow patterns inside and outside of the plasma torch:

(1) The flow in both the plasma torch region and jet region is quasi-steady, turbulent, having temperature-dependent properties;
(2) The plasma is in local thermodynamic equilibrium (LTE) state outside the electrode boundary layers and the jet fringes;
(3) The plasma is optically thin;
(4) The viscous dissipation and the pressure work terms in the energy equation are neglected due to the small Mach number;
(5) The plasma gas and the ambient gas into which the plasma jet is issued are the same (i.e., argon plasma jet is issued into argon);
(6) The cold-working gas (argon) is injected into the plasma torch in axial direction, i.e., without any swirling velocity component of the gas at the torch inlet;
(7) The induced electric field $\vec{V} \times \vec{B}$ is negligible in comparison with the applied electric field intensity E in the plasma arc region;
(8) Only the effect of the transversely injected cold carrier gas (argon) on the plasma jet is considered, i.e., the effect due to the particle injection is ignored (low particle loading rate).

2.2 Governing Equations

Based on the foregoing assumptions, the governing equations for the 3D, quasi-steady numerical simulations can be written in (r, θ, z) coordinates as follows:

Continuity equation:

$$\frac{1}{r}\frac{\partial}{\partial r}(r\rho v_r) + \frac{1}{r}\frac{\partial}{\partial \theta}(\rho v_\theta) + \frac{\partial}{\partial z}(\rho v_z) = 0 \qquad \text{(Eq 1)}$$

Momentum conservation equations:

r-direction (radial)

$$\begin{aligned}
&\rho\left(v_r\frac{\partial v_r}{\partial r} + \frac{v_\theta}{r}\frac{\partial v_r}{\partial \theta} + v_z\frac{\partial v_r}{\partial z}\right) \\
&= -\frac{\partial p}{\partial r} + \frac{\partial}{\partial r}\left(2\Gamma_u\frac{\partial v_r}{\partial r}\right) + \frac{1}{r}\frac{\partial}{\partial \theta}\left[\Gamma_u\left(\frac{1}{r}\frac{\partial v_r}{\partial \theta} + \frac{\partial v_\theta}{\partial r} - \frac{v_\theta}{r}\right)\right] \\
&\quad + \frac{\partial}{\partial z}\left[\Gamma_u\left(\frac{\partial v_r}{\partial z} + \frac{\partial v_z}{\partial r}\right)\right] \\
&\quad + \frac{2\Gamma_u}{r}\left(\frac{\partial v_r}{\partial r} - \frac{1}{r}\frac{\partial v_\theta}{\partial \theta} - \frac{v_r}{r}\right) + \rho\frac{v_\theta^2}{r} + F_r
\end{aligned} \qquad \text{(Eq 2)}$$

θ-direction (tangential)

$$\rho\left(v_r\frac{\partial v_\theta}{\partial r}+\frac{v_\theta}{r}\frac{\partial v_\theta}{\partial \theta}+v_z\frac{\partial v_\theta}{\partial z}\right)$$
$$=-\frac{1}{r}\frac{\partial p}{\partial \theta}+\frac{\partial}{\partial r}\left[\Gamma_u\left(\frac{\partial v_\theta}{\partial r}-\frac{v_\theta}{r}+\frac{1}{r}\frac{\partial v_r}{\partial \theta}\right)\right]$$
$$+\frac{1}{r}\frac{\partial}{\partial \theta}\left[2\Gamma_u\left(\frac{1}{r}\frac{\partial v_\theta}{\partial \theta}+\frac{v_r}{r}\right)\right]+\frac{\partial}{\partial z}\left[\Gamma_u\left(\frac{\partial v_\theta}{\partial z}+\frac{1}{r}\frac{\partial v_z}{\partial \theta}\right)\right]$$
$$+\frac{2\Gamma_u}{r}\left(\frac{1}{r}\frac{\partial v_r}{\partial \theta}+\frac{\partial v_\theta}{\partial r}-\frac{v_\theta}{r}\right)-rho\frac{v_r v_\theta}{r}+F_\theta \qquad \text{(Eq 3)}$$

z-direction (axial)

$$\rho\left(v_r\frac{\partial v_z}{\partial r}+\frac{v_\theta}{r}\frac{\partial v_z}{\partial \theta}+v_z\frac{\partial v_z}{\partial z}\right)=-\frac{\partial p}{\partial z}+\frac{1}{r}\frac{\partial}{\partial r}\left[\Gamma_u r\left(\frac{\partial v_z}{\partial r}+\frac{\partial v_r}{\partial z}\right)\right]$$
$$+\frac{1}{r}\frac{\partial}{\partial \theta}\left[\Gamma_u\left(\frac{1}{r}\frac{\partial v_z}{\partial \theta}+\frac{\partial v_\theta}{\partial z}\right)\right]+\frac{\partial}{\partial z}\left(2\Gamma_u\frac{\partial v_z}{\partial z}\right)+F_z \qquad \text{(Eq 4)}$$

Energy conservation equation:

$$\rho c_p\left(v_r\frac{\partial T}{\partial r}+\frac{v_\theta}{r}\frac{\partial T}{\partial \theta}+v_z\frac{\partial T}{\partial z}\right)$$
$$=\frac{1}{r}\frac{\partial}{\partial r}\left(r\Gamma_T\frac{\partial T}{\partial r}\right)+\frac{1}{r^2}\frac{\partial}{\partial \theta}\left(\Gamma_T\frac{\partial T}{\partial \theta}\right)+\frac{\partial}{\partial z}\left(\Gamma_T\frac{\partial T}{\partial z}\right)$$
$$-S_R+Q_{\text{current}} \qquad \text{(Eq 5)}$$

Potential equation:

$$\frac{1}{r}\frac{\partial}{\partial r}\left(r\sigma\frac{\partial \phi}{\partial r}\right)+\frac{1}{r^2}\frac{\partial}{\partial \theta}\left(\sigma\frac{\partial \phi}{\partial \theta}\right)+\frac{\partial}{\partial z}\left(\sigma\frac{\partial \phi}{\partial z}\right)=0 \qquad \text{(Eq 6)}$$

where p, T and ϕ are the gas pressure, temperature and the electric potential, v_r, v_θ and v_z are the velocity components, respectively.

In Eq 2-5, F_r, F_θ, F_z and Q_{current} represent the components of the Lorentz force vector F in r-, θ-, z-directions and the energy source term related to the current, respectively.

The Lorentz force can be expressed as

$$\vec{F}=\vec{j}\times\vec{B} \qquad \text{(Eq 7)}$$

where $\vec{B}$ is the self-induced magnetic induction intensity vector. The magnetic induction intensity can be calculated using the Biot-Savart law from the electric current density distribution, but a more effective numerical method is employed based on the solving of the magnetic vector potential equation, as discussed in (Ref 19-22). The electric current density vector j relates to the electric field intensity or electric potential ϕ as

$$\vec{j}=\sigma\vec{E}=-\sigma\nabla\phi \qquad \text{(Eq 8)}$$

The source term related to the current density appearing in Equation (5), Q_{current}, can be expressed as

$$Q_{\text{current}}=\frac{j_r^2+j_\theta^2+j_z^2}{\sigma}+\frac{5}{2}\frac{k_B}{e}\vec{j}\cdot\nabla T \qquad \text{(Eq 9)}$$

where k_B and e are Boltzmann constant and the elementary charge, respectively, whereas j_r, j_θ and j_z are the components of the current density vector j in r-, θ- and z-directions, respectively.

In the plasma jet region, any contributions from current flow can be neglected because the anode arc-root attachments locate far away from the anode nozzle exit in this study (Ref 54). Therefore, in the plasma jet region, the potential equation (Eq 6) is not necessary, and the source terms related to the current density in the momentum and energy conservation equations are zero, i.e., $F_r=F_\theta=F_z=0$ and $Q_{\text{current}}=0$.

The standard $K-\varepsilon$ two-equation turbulence model is employed in this study. The turbulent kinetic energy and its dissipation rate equations are

$$\frac{\partial}{\partial z}(\rho v_z K)+\frac{1}{r}\frac{\partial}{\partial r}(\rho v_r r K)+\frac{1}{r}\frac{\partial}{\partial \theta}(\rho v_\theta K)$$
$$=\frac{\partial}{\partial z}\left(\Gamma_K\frac{\partial K}{\partial z}\right)+\frac{1}{r}\frac{\partial}{\partial r}\left(r\Gamma_K\frac{\partial K}{\partial r}\right)$$
$$+\frac{1}{r^2}\frac{\partial}{\partial \theta}\left(\Gamma_K\frac{\partial K}{\partial \theta}\right)+G-\rho\varepsilon \qquad \text{(Eq 10)}$$

$$\frac{\partial}{\partial z}(\rho v_z \varepsilon)+\frac{1}{r}\frac{\partial}{\partial r}(\rho v_r r\varepsilon)+\frac{1}{r}\frac{\partial}{\partial \theta}(\rho v_\theta \varepsilon)$$
$$=\frac{\partial}{\partial z}\left(\Gamma_\varepsilon\frac{\partial \varepsilon}{\partial z}\right)+\frac{1}{r}\frac{\partial}{\partial r}\left(r\Gamma_\varepsilon\frac{\partial \varepsilon}{\partial r}\right)$$
$$+\frac{1}{r^2}\frac{\partial}{\partial \theta}\left(\Gamma_\varepsilon\frac{\partial \varepsilon}{\partial \theta}\right)+\frac{\varepsilon}{K}(c_1G-c_2\rho\varepsilon) \qquad \text{(Eq 11)}$$

The turbulent generation term G appearing in Eq 10 and 11 are expressed as

$$G=\mu_t\left\{2\left[\left(\frac{\partial v_z}{\partial z}\right)^2+\left(\frac{\partial v_r}{\partial r}\right)^2+\left(\frac{1}{r}\frac{\partial v_\theta}{\partial \theta}+\frac{v_r}{r}\right)^2\right]+\left(\frac{\partial v_z}{\partial r}+\frac{\partial v_r}{\partial z}\right)^2\right.$$
$$\left.+\left(\frac{\partial v_\theta}{\partial z}+\frac{\partial v_z}{r\partial \theta}\right)^2+\left(\frac{1}{r}\frac{\partial v_r}{\partial \theta}+\frac{\partial v_\theta}{\partial r}-\frac{v_\theta}{r}\right)^2\right\} \qquad \text{(Eq 12)}$$

All the physical quantities in the foregoing equations are their time-averaged values. ρ, σ and S_R are the temperature-dependent mass density, electric conductivity and the optically thin radiation loss per unit volume of argon plasmas, respectively. The effective 'diffusion' coefficients are the combination of laminar and turbulent values, i.e.

$$\Gamma_u=\mu+\mu_t;\ \Gamma_T=k+\mu_t c_p/\text{Pr}_t;$$
$$\Gamma_K=\mu+\mu_t/\sigma_K;\ \Gamma_\varepsilon=\mu+\mu_t/\sigma_\varepsilon \qquad \text{(Eq 13)}$$

where μ, k, c_p are the temperature-dependent molecular viscosity, thermal conductivity and specific heat at constant pressure of the plasma, respectively. μ_t is the turbulent viscosity ($\mu_t=\rho\, c_\mu K^2/\varepsilon$), c_1, c_2, c_μ, Pr_t, σ_K and σ_ε are model constants, equal to 1.44, 1.92, 0.09, 0.9, 1.0 and 1.3, respectively, in the K-ε turbulent model.

2.3 Computational Domain and Boundary Conditions

As shown in Fig. 3, the whole computational domain, with its geometrical dimensions, is composed of two subregions, i.e., the torch region and the jet region, which are formed by the rotation of the region ABCDEFGHA and

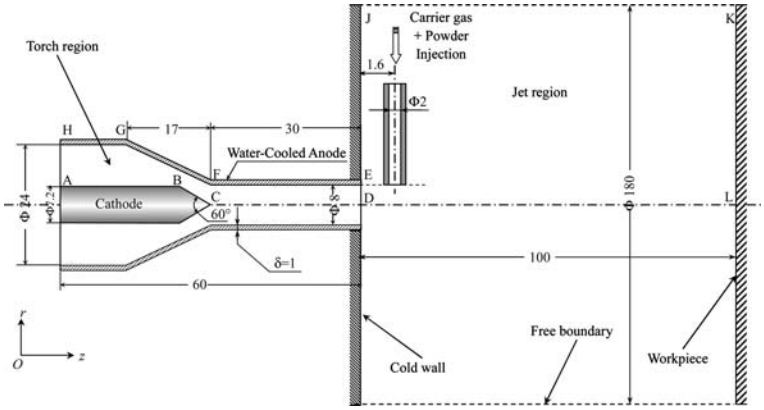

Fig. 3 Calculation domain

DEJKLD about the torch axis, respectively. The injection tube, with an inner diameter of 2.0 mm, is located 1.8 mm downstream of the anode nozzle exit. In previous papers, the methods for 3D modeling of DC arc plasma torches (Ref 21) and plasma jets (Ref 49) have been described in detail, which will not be repeated here. In this study, the same method, also with the same working parameters and boundary conditions as those presented in Ref. (21), is employed to simulate the 3D characteristics of arc plasmas in the torch region. For determining the location of the anode arc-root attachment in steady state, 1 mm thick anode region is included in the calculation domain. The axial location of the arc root attachment is determined by using the Steenbeck's minimum principle (Ref 23), which postulates a minimum arc voltage for a given arc current, working gas flow rate, and torch configuration. The non-uniform arc-root attachment in the circumferential direction along the anode inner surface is determined by calculation itself. In the jet region, similar method and boundary conditions as those presented in Ref. (49) are used, except for the boundary conditions at the inlet of the jet region (DE). In this study, the calculated non-axisymmetric profiles for temperature (T), velocity ($\overline{v}$), turbulent kinetic energy (K), and its dissipation rate (ε) at the exit of the anode nozzle are employed as the starting boundary conditions for modeling of the plasma jet.

3. Modeling Approach: Particle Movement and Heating

In this study, the following assumptions are employed for study of the particle behavior: (1) spherical metal (nickel) particles are studied, i.e., the pertinent Biot number is small (e.g., less than 0.01) so that the temperatures within the particle can be treated as everywhere uniform; (2) the effect of injected particles on the plasma jet characteristics and the particle-particle interaction are negligible, which is reasonable for the case of low-particle loading rate; (3) the mean magnitude of the plasma turbulent fluctuating velocity remains unchanged within each of the eddies before the eddy vanishes; (4) the loading rate of particles is low; (5) the effects of the vapor contamination from an intensely evaporating particle (if any) on particle behavior and the physical properties of the plasma jet are negligible; (6) the injection velocity of particles is the same as the carrier gas velocity at the exit section of the injection tube.

Based on the preceding assumptions, the motion and heating of a single particle, including its diameter variation with time if evaporation occurs, inside the plasma jet are calculated using the approach presented in Section 3.2 of Ref. (49). Under thermal plasma conditions in the turbulent regime, the following factors affecting the particle heat transfer and drag force are considered: (i) appreciable property variation within the boundary layer around the particle due to the large temperature difference between the particle surface and the local plasma flow; (ii) the turbulent fluctuations; (iii) the Knudsen and evaporation (if any) effects; and (iv) particle thermophoresis.

4. Modeling Results and Discussions

4.1 Description of the Computational Method

In this study, the SIMPLE-like algorithm (Ref 55) has been employed to solve simultaneously the non-linear Eq 1-5, 6 [for torch region only], (10) and (11) with the new version of the non-commercial software FAST-3D (Fluid Analytical Simulation Tools—Three Dimensional) (Ref 56). The detailed description of the features of this modified computer code, FAST-3D, was presented in Ref. (49). 3D, body-fitted, non-uniform meshes $32(z) \times 22(r) \times 11(\theta)$ and $42(z) \times 32(r) \times 42(\theta)$ for the modeling of temperature and flow fields in the torch region and jet region, respectively, are employed in this paper. The grid mesh in $z-r$ plane is shown in Fig. 4. The mesh in θ-direction is uniform from 0 through 2π . In this study, firstly, the 3D temperature and flow fields are simulated using the $32(z) \times 22(r) \times 11(\theta)$ non-uniform mesh; and secondly, the 3D heat transfer and flow patterns in the plasma jet region are simulated using the $42(z) \times 32(r) \times 42(\theta)$

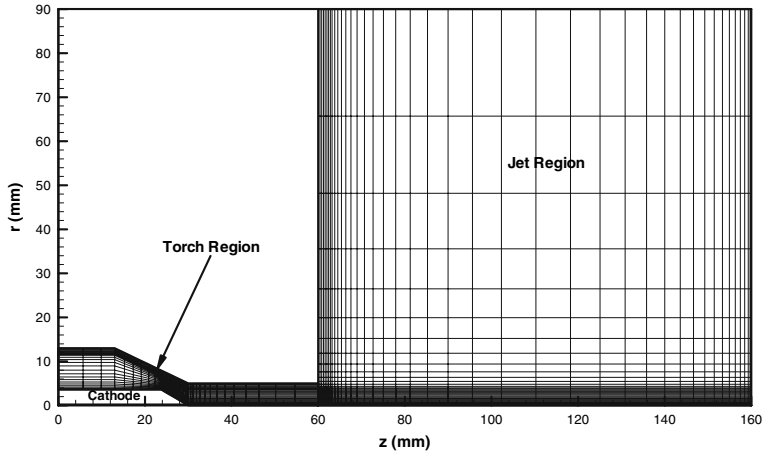

Fig. 4 Mesh generation in the torch region $[32(z) \times 22(r) \times 11(\theta)]$ and jet region $[42(z) \times 32(r) \times 42(\theta)]$

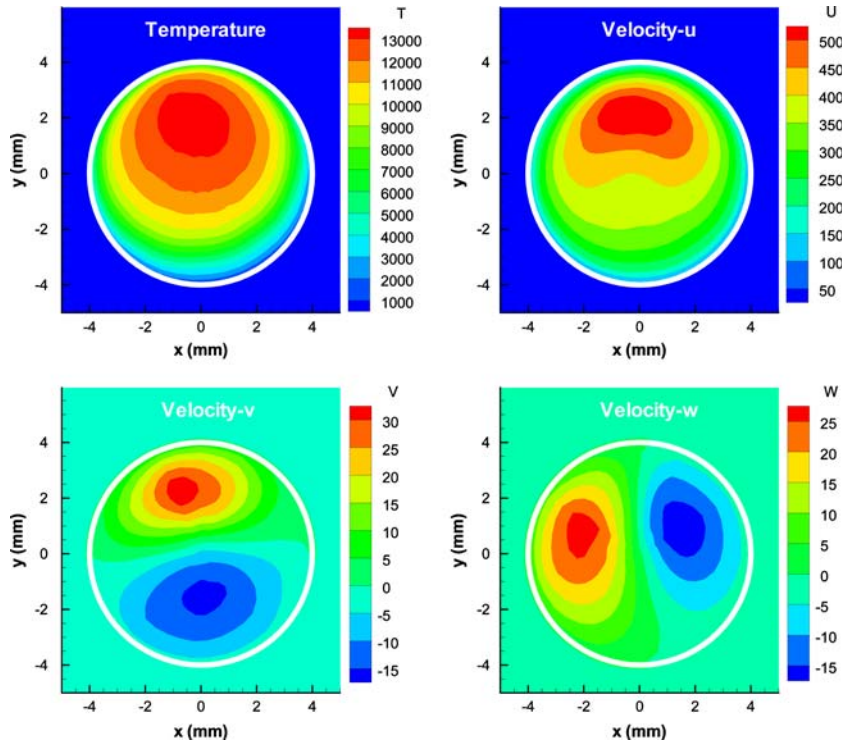

Fig. 5 The calculated contours of temperature and velocity components in x-, y- and z-directions at the outlet of the anode nozzle ($I = 400$ A and $Q = 2.0$ STP m^3/h)

non-uniform mesh with the calculated distributions of temperature and flow fields at the torch nozzle exit as the starting boundary conditions.

4.2 Results and Discussion

In this section, the influences of arc current, working gas flow rate, as well as the injection velocity of the carrier gas, on the heat and flow patterns of the plasma arc and/or jet are studied. The trajectories and heating histories of nickel particles with different diameters are also predicted based on the calculated temperature and flow fields in the jet region.

4.2.1 3D Temperature and Flow Fields in the Torch and Jet Regions without Cold Carrier Gas Injection. As discussed in Section 1, due to the lack of axial symmetry distributions of temperature, velocity, turbulent kinetic energy and its dissipation rate at the exit of the anode nozzle, the temperature and flow fields in the jet region would be 3D even with no transverse carrier gas injection. The contours of temperature and velocity components in x-, y- and z-directions at the outlet of the anode nozzle for the case of $I = 400$ A and $Q = 2.0$ STP m^3/h are shown in Fig. 5, where the white circle indicates the inner surface of the anode nozzle. Although the governing equations

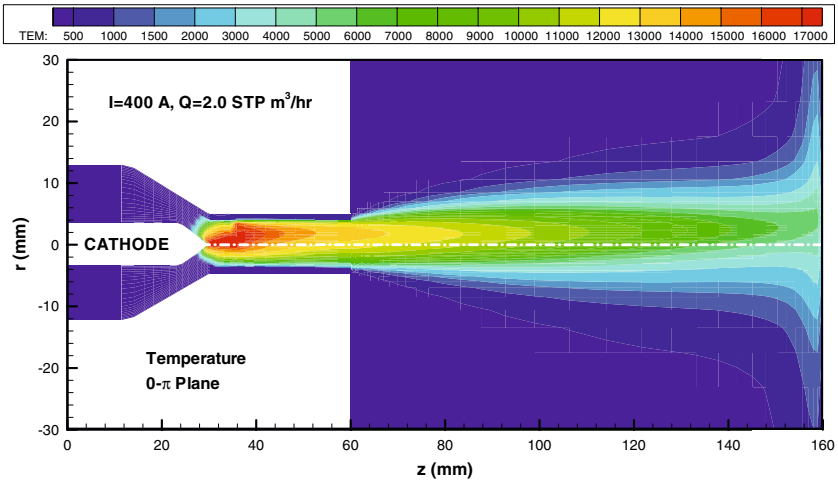

Fig. 6 The temperature distributions in both torch and jet regions in 0-π plane without cold-carrier gas injection ($I = 400$ A and $Q = 2.0$ STP m^3/h)

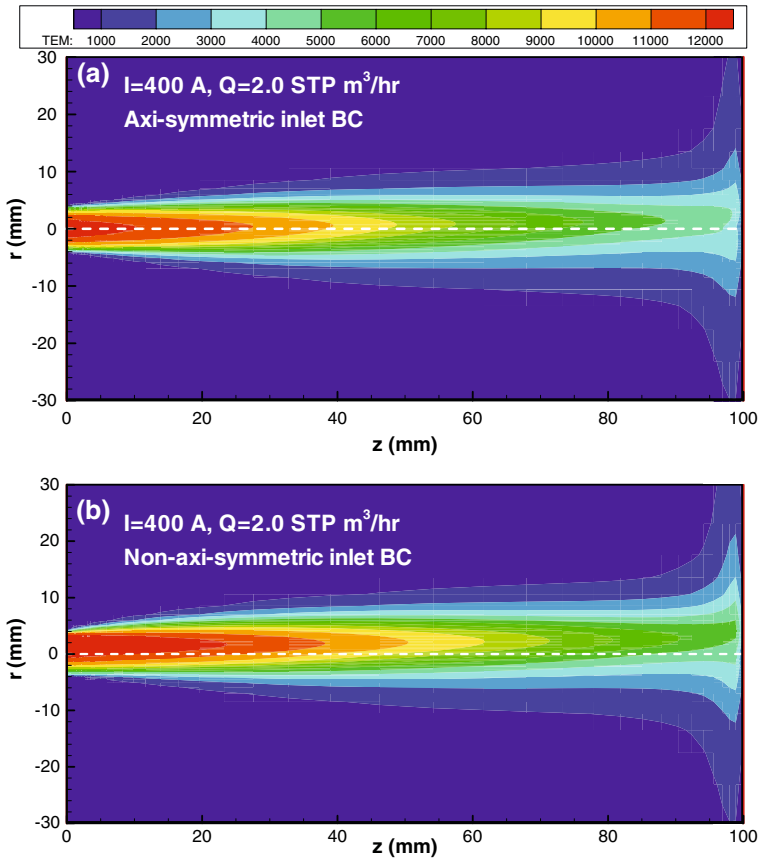

Fig. 7 Comparison of the calculated temperature distributions in 0-π plane in the jet region with axi-symmetric (a) and non-axi-symmetric (b) inlet boundary conditions ($I = 400$ A and $Q = 2.0$ STP m^3/h)

presented in Section 2 are in the form of cylindrical coordinates, the computer code, FAST-3D, can convert these equations into the corresponding form in Cartesian coordinates (Ref 56). The calculated temperature distributions in a plane where the anode arc root stays, which are the so-called 0-π plane in Ref. (21), are shown in Fig. 6. From Fig. 5 and 6, it can be seen that not only the temperature and flow fields inside the plasma torch are 3D because of the local attachment of the anode arc-root on the anode inner surface, but these 3D features are also

transferred to the plasma jet region, even no transverse cold carrier gas injection is imposed. For verifying the 3D features in the jet region due to the non-axi-symmetric heat and flow patterns at the exit of the torch anode, a numerical experiment is conducted as follows: (1) the calculated mass-averaged temperature, axial-velocity component, turbulent kinetic energy and its dissipation rate, with zero radial and tangential velocity components, are used as the boundary conditions at the beginning of the jet region; (2) other conditions are the same as those in the case shown in Fig. 6. Because the mass-averaged temperature and axial velocity component are nearly axi-symmetric (Ref 21), the calculated temperature distribution in the plasma jet region is also nearly axi-symmetric, as shown in Fig. 7(a). Compared with the results with non-axi-symmetric inlet boundary conditions, as shown in Fig. 7(b), there are substantial deviations from axial symmetry. The calculated results show that: (1) the corresponding deflection angles of the plasma jets from their geometrical axis are 0.8° and 1.8°, respectively; (2) the corresponding lengths of the high-temperature region, defined as the largest axial distance of the isotherm of 7,000 K, are also different, which are 66 mm and 80 mm, respectively, for these two cases.

Similar calculated results for $I = 600$, $Q = 2.0$ STP m^3/h and $I = 800$ A, $Q = 2.1$ STP m^3/h are shown in Fig. 8 and 9, respectively. The calculated deflection angles of the jet from its geometrical axis (α) and the lengths of high-temperature regions in the jet (L_{jet}) are listed in Table 1. From Fig. 6, 8, 9 and Table 1, it can be concluded that: (a)

Table 1 The calculated deflection angle of the plasma jet from its geometrical axis and the length of high-temperature region of the plasma jet without cold carrier gas injection

I, A	Q, STP m^3/h	α (°)	L_{jet}, mm
400	2.0	1.8	80.0
600	2.0	1.6	90.0
800	2.1	0.3	91.0

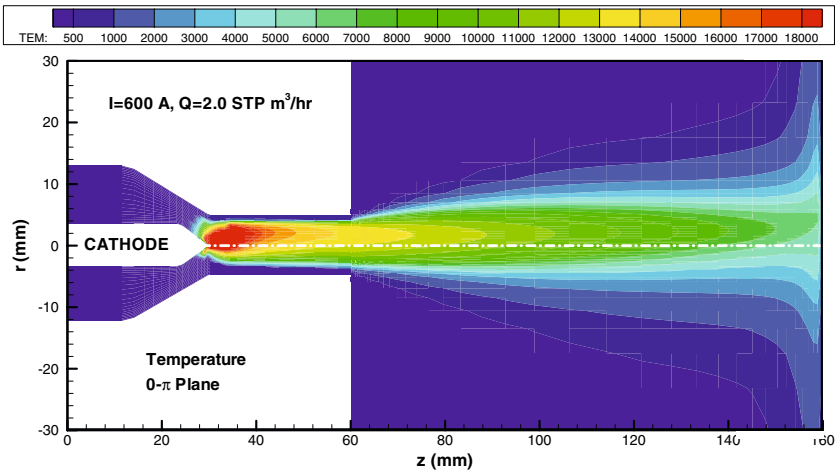

Fig. 8 The temperature distributions in the torch and jet regions in 0-π plane without cold carrier gas injection ($I = 600$ A and $Q = 2.0$ STP m^3/h)

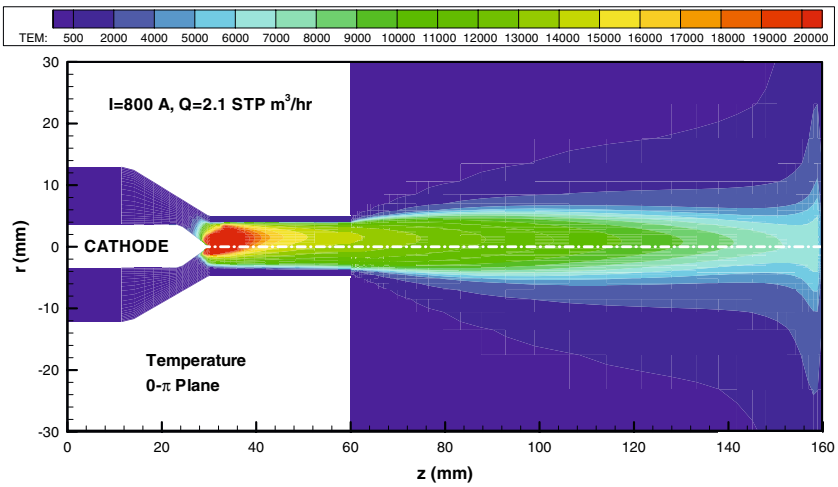

Fig. 9 The temperature distributions in the torch and jet regions in 0-π plane without cold carrier gas injection ($I = 800$ A and $Q = 2.1$ STP m^3/h)

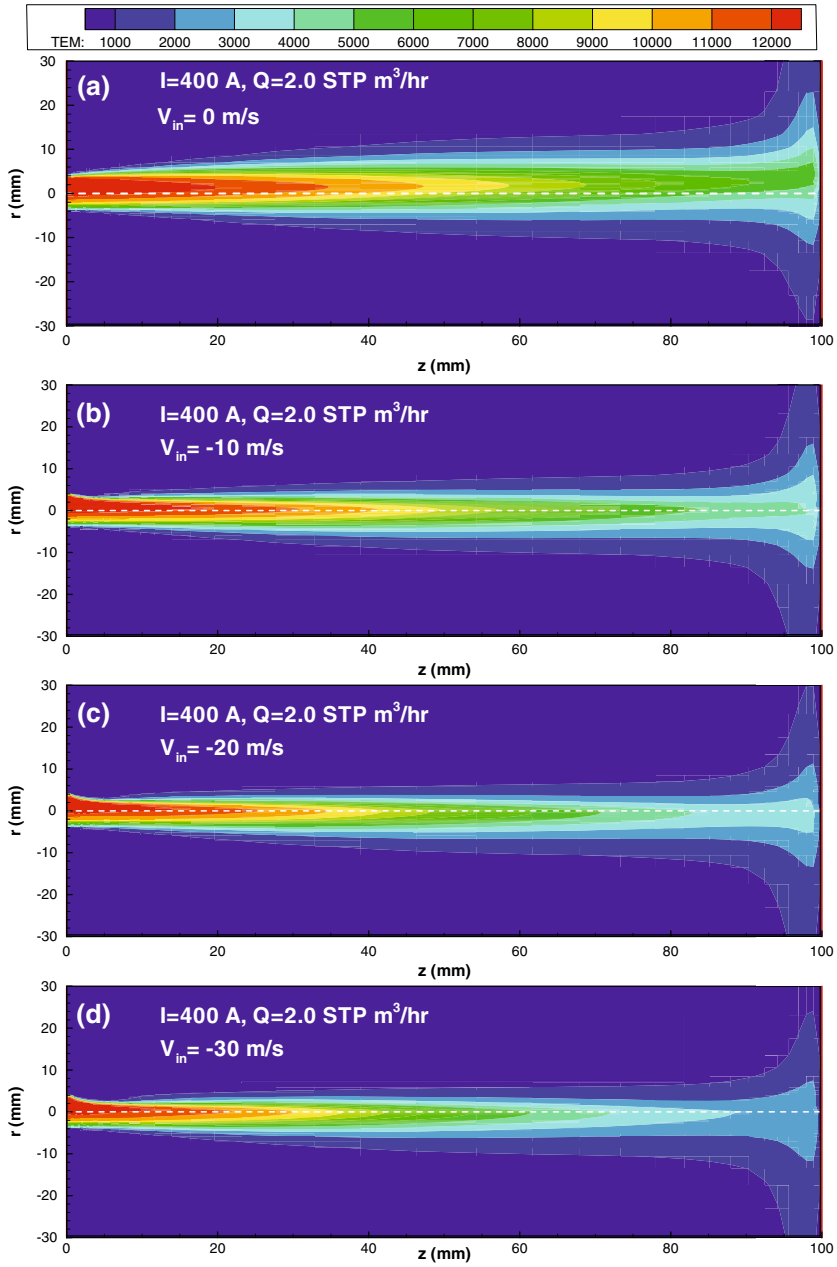

Fig. 10 The computed isotherms in the injection plane in the jet region for different carrier gas injection velocities ($I = 400$ A and $Q = 2.0$ STP m^3/h)

with an increase of the arc current, the anode arc-root attachment will move upstream due to the enhanced magnetic body force, leading to a shorter arc, but higher-maximum temperatures and axial velocities at the exit of the anode nozzle, as well as to a stronger penetration effect of the main plasma stream due to the increase of temperature, resulting in a longer high temperature region in the jet; (b) with an increase of the plasma working gas flow rate, the anode arc-root attachment will move downstream due to the enhanced gasdynamic drag force, leading to higher maximum temperatures and axial velocities at the exit of the anode nozzle (Ref 21), as well as to stronger mixing effects of the plasma main stream with the environment, resulting in a shorter high temperature region in the jet.

4.2.2 3D Temperature and Flow Fields in the Torch and Jet Regions with Cold Carrier Gas Injection. As expected, with the transverse injection of the cold-carrier gas, the plasma jet emanating from the anode nozzle will be deflected from its original direction (Ref 48-50). For simplicity, we define in this section:

(1) Characteristic axis of the plasma jet: the line passing through the center point of the nozzle exit and the point of largest axial extension of the 7,000 K isotherm.

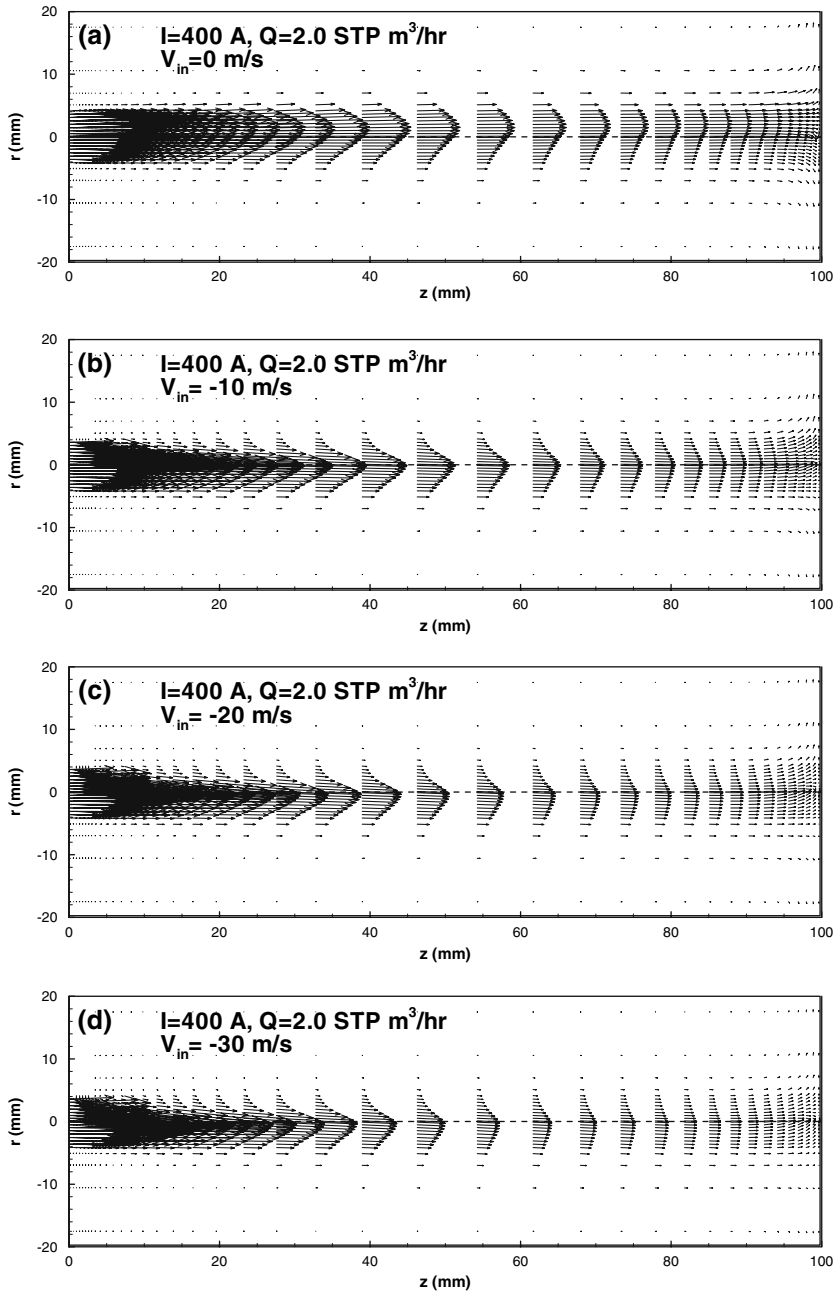

Fig. 11 The computed distributions of velocity vectors in the injection plane within the jet region for different carrier gas injection velocities ($I = 400$ A and $Q = 2.0$ STP m^3/h)

(2) Referenced characteristic axis of the plasma jet: the characteristic axis of the plasma jet without carrier gas injection.
(3) Injection plane: the plane formed by the plasma torch axis and injection tube axis.

For the case of $I = 400$ A, $Q = 2.0$ STP m^3/h, and $V_{in} = 0$, -10, -20, -30 m/s, with the corresponding volumetric flow rates of 0, 0.113, 0.226, and 0.339 STP m^3/h, respectively, the calculated isotherms in the injection plane within the plasma jet region are shown in Fig. 10. The corresponding calculated-deflection angles ($\Delta\alpha$) of the plasma jet from its referenced characteristic axis are 0°, 1.7°, 1.9°, and 2.0°, respectively. It can be seen that the variations of the deflection angles are small with increasing carrying gas injection velocity. But the calculated corresponding lengths of the high-temperature isotherms change substantially (80.0, 65.0, 54.0 and 47.6 mm, respectively). This is due to the cooling effect of the cold carrier gas. The corresponding calculated distributions of velocity vectors in the injection plane are shown in Fig. 11.

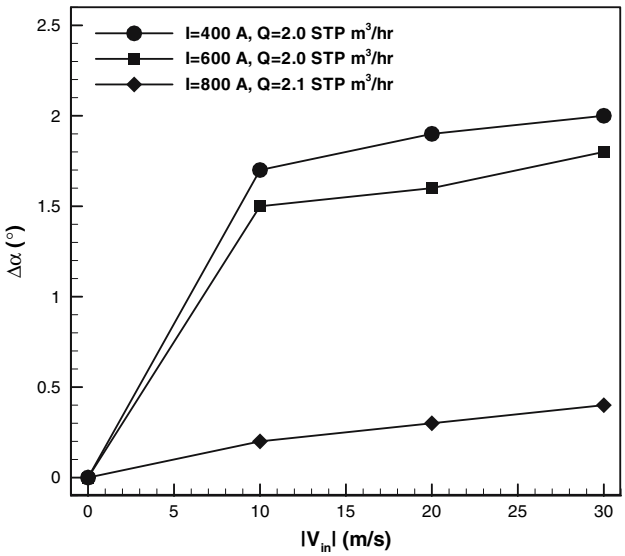

Fig. 12 The calculated deflection angles of the jet characteristic axis from its referenced characteristic axis in the injection plane for the plasma jets

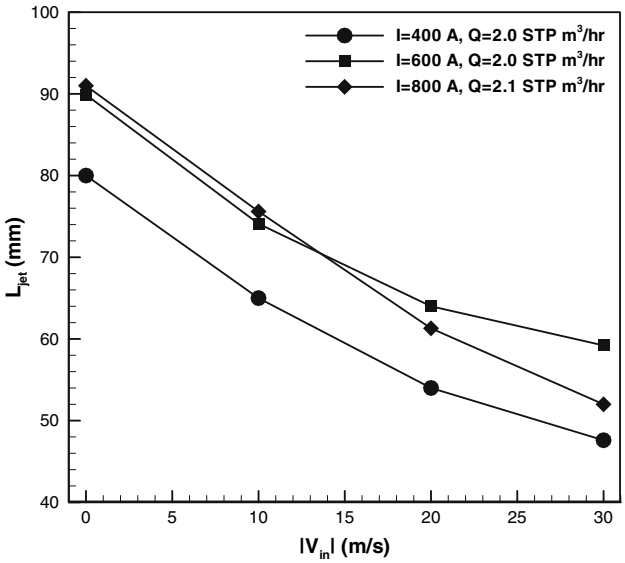

Fig. 13 The calculated lengths of the high-temperature region in the injection plane for the plasma jets

For the cases of $I = 400$, 600 and 800 A and $Q = 2.0$, 2.1 STP m^3/h with $V_{in} = 0$, −10, −20, −30 m/s, the calculated deflection angles ($\Delta\alpha$) and high-temperature region lengths (L_{jet}) are shown in Fig. 12 and 13, respectively. Figures 12 and 13 show that: (a) the injection of the cold carrier gas has a much more significant effect on the lengths of the high-temperature region than on the deflection angles of the plasma jet; (b) increasing the velocity of the carrier gas results in small increments of the deflection angle of the plasma jet when the injection velocity of the carrier gas is larger than 10 m/s; while (c) the rate of the length changes of the high temperature region just slightly decreases with increasing carrier gas injection velocity for all the cases studies in this paper.

4.2.3 Trajectories and Heating Histories of Sprayed Nickel Particles. As indicated in Ref. (49), even for particles with the same particle diameter, same injection velocity and same injection location, different particles will follow different trajectories and heating histories due to the influence of random turbulent fluctuations. In this paper, nickel particles with diameters of 5 and 10 μ m are used to study the trajectories and heating histories of such particles injected into the high-temperature plasma jet region, although in plasma spraying larger particles (greater/equal to 40 μm) are commonly used. The sampling particle number is $N_p = 5000$, which is enough for correctly predicting the particle spatial distributions (Ref 49). Particle dispersion is studied here based on the calculated turbulent flow field using the two-equation (k-ε) turbulence model. For the case of $I = 400$ A, $Q = 2.0$ STP m^3/h and $V_{in} = -10$ m/s, the particle trajectories and heating histories for nickel particles with all initial diameter of 10 μ m are shown in Fig. 14(a) and (b), respectively. The predicted dispersions of the sprayed particles at extended-different axial locations ($z = 85$, 110, 135 and 159 mm) are plotted in Fig. 15, where $z = 159$ mm may be the cross section very close to the substrate. The arrows indicate the injection direction of the carrier gas and the particles.

The parameters of particles in motion (such as their temperatures, velocities, spatial distributions, etc.) just before impinging on the substrate are very important since they will affect directly the formation of coatings and the coating qualities (Ref 57). In this section, parameters concerning the statistical characteristics of the dispersed particles are defined as follows:

$$\bar{x}_p = \sum x_{p\cdot i}/N_p, \bar{y}_p = \sum y_{p\cdot i}/N_p, \quad \text{and } \bar{r}_p = \sqrt{\bar{x}_p^2 + \bar{y}_p^2} \tag{Eq 14}$$

$$\sigma_p = \sqrt{\frac{\sum \left(x_{p,i} - \bar{x}_p\right)^2 + \left(y_{p,i} - \bar{y}_p\right)^2}{N_p}} \tag{Eq 15}$$

$$\bar{T}_p = \sum T_{p,i}/N_p, \quad \sigma_T = \sqrt{\frac{\sum \left(T_{p,i} - \bar{T}_p\right)^2}{N_p}} \tag{Eq 16}$$

$$\bar{D}_p = \sum D_{p,i}/N_p, \quad \sigma_D = \sqrt{\frac{\sum \left(D_{p,i} - \bar{D}_p\right)^2}{N_p}}]] > \tag{Eq 17}$$

where $x_{p,i}$, $y_{p,i}$, $T_{p,i}$ and $D_{p,i}$ indicate the x-, y-position, temperature and diameter of the ith particle at a certain axial (z) position, $\bar{x}_p$, $\bar{y}_p$, $\bar{T}_p$ and $\bar{D}_p$ represent the averaged x-, y-position, averaged temperature and averaged diameter of particles at a certain axial (z) position, respectively, $\bar{r}_p$ indicates the corresponding averaged radial position with reference to the jet geometrical axis, while σ_p, σ_T and σ_D (the standard deviations of the

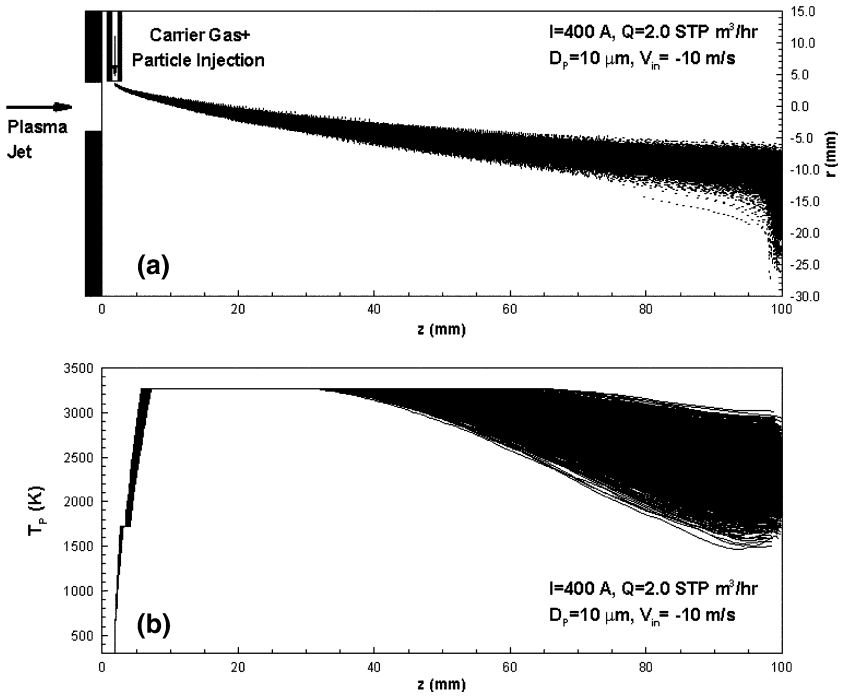

Fig. 14 Predicted particle moving trajectories (a) and heating histories (b) of dispersed nickel particles in the injection plane with all initial diameter of 10 μm for the case of $I = 400$ A, $Q = 2.0$ STP m^3/h and $V_{in} = -10$ m/s

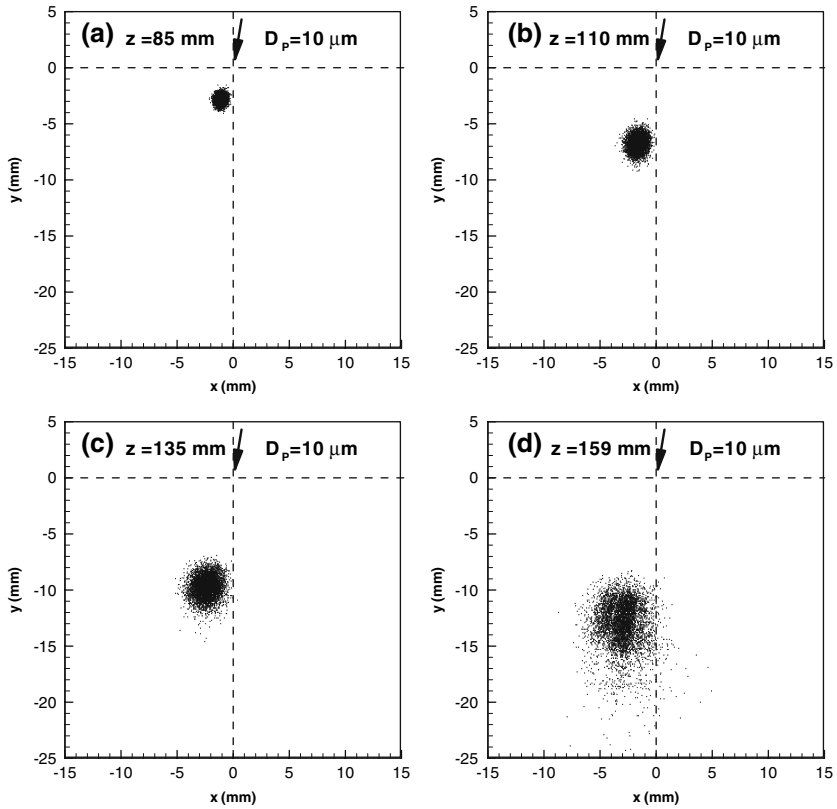

Fig. 15 Predicted dispersed particle distributions at four extended sections with all initial diameter of 10 μm for the case of $I = 400$ A, $Q = 2.0$ STP m^3/h and $V_{in} = -10$ m/s

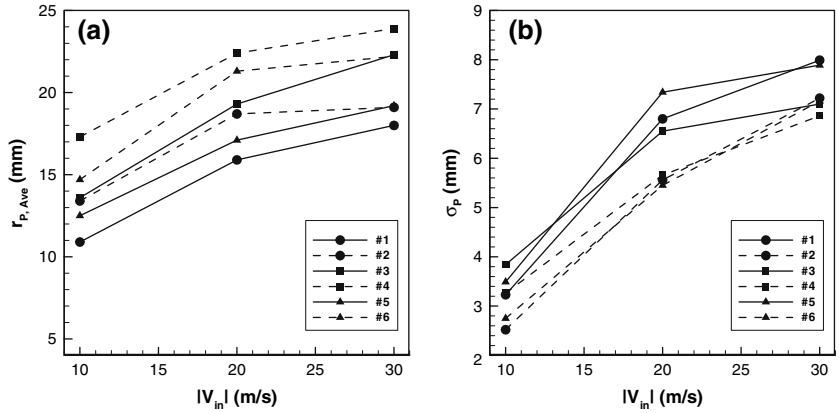

Fig. 16 The predicted averaged radial position (a) and the corresponding characteristic pattern radius (b) of turbulent dispersed particles at $z = 159$ mm in the plasma jet region

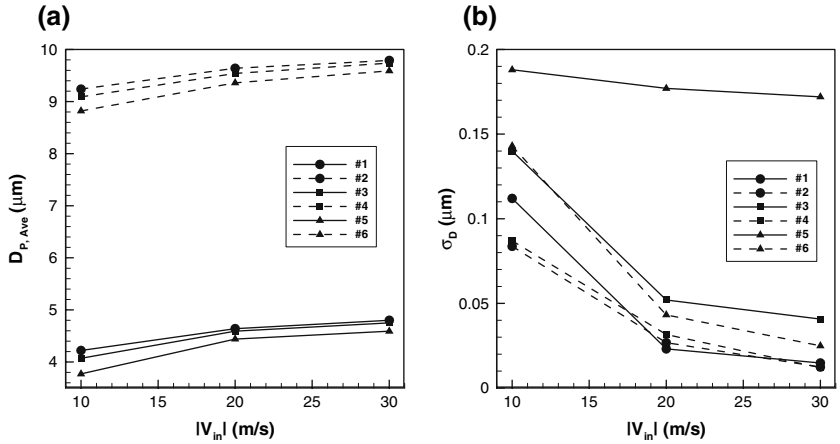

Fig. 17 The predicted averaged particle diameter (a) and the corresponding characteristic diameter range (b) of turbulent dispersed particles at $z = 159$ mm in the plasma jet region

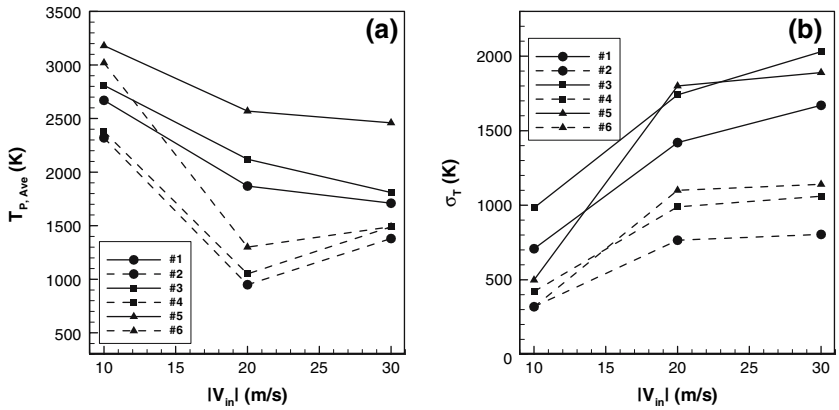

Fig. 18 The predicted averaged particle temperature (a) and the corresponding characteristic temperature range (b) of turbulent dispersed particles at $z = 159$ mm in the plasma jet region

Table 2 Case list studied in Fig. 16-18

Case #	I, A	Q, STP m^3/h	D_p, μm
1	400	2.0	5.0
2	400	2.0	10.0
3	600	2.0	5.0
4	600	2.0	10.0
5	800	2.1	5.0
6	800	2.1	10.0

particle position, surface temperature, and diameter) are the so-called characteristic pattern radius, characteristic temperature range, and characteristic diameter range of particle dispersions, respectively. Small values of σ_p, σ_T and σ_D indicate less dispersions of particles and more uniform particle temperatures and sizes before they impinge on the substrate within the turbulent plasma jet region. The calculated statistical parameters (Eq 14-17) at $z = 159$ mm in the jet region are shown in Fig. 16-18, where the lines indicated by #1∼#6 represent the cases listed in Table 2. By analyzing the calculated results presented in Fig. 16-18, it can be concluded that: (1) by increasing the particle initial diameter or the injection velocity of the cold carrier gas, while keeping the other parameters constant, the particles will have a deeper penetration depth (i.e., a larger value of $\bar{r}_p$) and larger spatial dispersion range due to the larger inertia of particles and/or the additional momentum from the carrier gas injection, while the spatial dispersion range increases (i.e., a larger value of σ_p) with the increase of the injection velocity of the cold-carrier gas and the decrease of the particle initial diameter; (2) in this study, the smaller values of $\bar{r}_p$ and σ_p indicate that most of the particles concentrate near the high temperature core region of the plasma jet, which leads to higher averaged particle temperatures ($\bar{T}_p$) with a smaller corresponding particle characteristic temperature range (σ_T). In addition, there will be significant particle evaporation (i.e., smaller averaged particle diameter, $\bar{D}_p$, and a larger corresponding particle characteristic diameter range σ_D).

5. Concluding Remarks

In this paper, the 3D characteristics of heat transfer and flow patterns in an atmospheric-pressure thermal plasma spray process in the steady mode of operation is simulated, including both the plasma torch region and the plasma jet region. The sprayed nickel particles, together with the cold-carrier gas, are injected transversely into the plasma jet region. The corresponding heating histories and 3D trajectories of nickel powders are also predicted based on the calculated 3D temperature and flow fields. Main conclusions obtained from the present study are as follows:

(1) The 3D features of the heat transfer and flow patterns inside the thermal plasma torch are significant due to the constricted, local anode arc-root attachment on the anode inner surface. And this 3D feature also leads to 3D temperature and flow fields in the plasma jet region, even with no transverse carrier gas injection. Therefore, the 3D heat and flow patterns of the plasma jet in actual thermal plasma spraying result not only from the transverse injection of the cold carrier gas, but also from the non-axi-symmetric distributions at the exit of the plasma torch.

(2) Due to the 3D temperature and flow fields in the plasma jet region, the trajectories of sprayed particles are also 3D, which depends on both the plasma torch operation parameters and the initial injection velocity and initial diameter of particles. Thus, optimized combinations of plasma torch operation parameters, carrier gas injection velocity, sprayed particle diameter, etc., are necessary for obtaining high quality coatings.

Although in the present paper, metallic (nickel) particles are employed for simplifying the calculation of the particle heating histories, and the action of heated and accelerated particles on the plasma jet is also neglected, this study can be extended to the cases with high-loading rate of non-metallic particles, with further development and by coupling the heat conduction equation within the particles with the temperature and flow field calculation and including the particle-plasma interaction terms in the mass, momentum and energy conservation equations (Ref 32, 58). And distributions of particle sizes, velocity, location and flow direction of particles can also be considered in future studies. Furthermore, the present model does not cover the complicated large-eddy or non-isotropic turbulent processes within the plasma jet. With the development of computer hardware and software in the future, the large-scale large-eddy simulation (LES) and/or direct numerical simulation (DNS) may become feasible based on parallel, supercomputing platforms for studying the spatial/temporal distributions of thermal plasmas in turbulent regime. Finally, it should be emphasized that since the DC arc plasma torch usually works in restrike or takeover mode in actual thermal plasma spray process, thus, the simulations on the time-dependent, 3D heat transfer and flow patterns inside and outside of the plasma torch, as well as the enhancement of turbulent mixing of the unsteady plasma jet with the surrounding gas, are necessary for providing more helpful information on the actual plasma spray process in future work.

Acknowledgment

This work has been supported through a postdoctoral fellowship from the Department of Mechanical Engineering, University of Minnesota, and by the National Natural Science Foundation of China grant #10405015. The support through a supercomputer grant by the University of Minnesota Supercomputing Institute is gratefully acknowledged.

References

1. P. Fauchais and A. Vardelle, Pending Problems in Thermal Plasmas and Actual Development, *Plasma Phys. Contr. Fusion*, 2000, **42**(12, Suppl. B), p B365-B383

2. D.A. Scott, P. Kovitya, and G.N. Haddad, Temperatures in the Plume of a DC Plasma Torch, *J. Appl. Phys.*, 1989, **66**(11), p 5232-5239
3. A.H. Dilawari, J. Szekely, and R. Westhoff, An Assessment of the Heat and Fluid Flow Phenomena Inside Plasma Torches in Non-transferred Arc Systems, *ISIJ Int.*, 1990, **30**(5), p 381-389
4. R. Westhoff and J. Szekely, A Model of Fluid, Heat Flow, and Electromagnetic Phenomena in a Nontransferred Arc Plasma Torch, *J. Appl. Phys.*, 1991, **70**(7), p 3455-3466
5. R. Westhoff, A.H. Dilawari, and J. Szekely, A Mathematical Representation of Transport Phenomena Inside a Plasma Torch, *Mat. Res. Soc. Symp. Proc.*, 1991, **190**, p 213-219
6. A.B. Murphy and P. Kovitya, Mathematical Model and Laser-Scattering Temperature Measurements of a Direct-Current Plasma Torch Discharging into Air, *J. Appl. Phys.*, 1993, **73**(10), p 4759-4769
7. A. Bouvier, C. Delalondre, O. Simonin, and J. Brilhac, Numeric Modelling of the Internal Behaviour of a Vortex Stabilized Plasma Torch, *International Symposium on Heat & Mass Transfer Under Plasma Conditions*. Cesme, Turkey, 1994, p 79-89
8. J.M. Bauchire, J.J. Gonzalez, and A. Gleizes, Modeling of a DC Plasma Torch in Laminar and Turbulent Flow, *Plasma Chem. Plasma Process.*, 1997, **17**(4), p 409-432
9. S.A. Wutzke, ''Conditions Governing the Symptomatic Behavior of an Electric Arc in a Superimposed Flow Field'', Ph. D. Thesis, Department of Mechanical Engineering, University of Minnesota, 1967
10. Lan Yu, ''Modelling of D. C. Arc Plasma Torches and Jets'', Master Thesis, Department of Engineering Mechanics, Tsinghua University, 1997 (In Chinese)
11. Peng Han, ''Numerical and Experimental Studies on the Characteristics of D. C. Arc Plasma Torches and Jets'', Ph. D. Thesis, Department of Engineering Mechanics, Tsinghua University, 1999 (In Chinese)
12. He-Ping Li, ''Studies of Heat Transfer and Fluid Flow in a D. C. Arc Plasma Torch and Plasma Jet'', Ph. D. Thesis, Department of Engineering Mechanics, Tsinghua University, 2001 (In Chinese)
13. A. Kaddani, S. Zahrai, C. Delalondre, and O. Simonin, Three-Dimensional Modelling of Unsteady High-Pressure Arcs in Argon, *J. Phys. D: Appl. Phys.*, 1995, **28**, p 2294-2305
14. G. Speckhofer and H.-P. Schmidt, Experimental and Theoretical Investigation of High-Pressure Arcs—Part II: The Magnetically Deflected Arc (Three-Dimensional Modeling), *IEEE T. Plasma Sci.*, 1996, **24**(4), p 1239-1248
15. L.Z. Schlitz, S.V. Garimella, and S.H. Chan, Gas Dynamics and Electromagnetic Processes in High-Current Arc Plasmas, Part II. Effects of External Magnetic Fields and Gassing Materials, *J. Appl. Phys.*, 1999, **85**(5), p 2547-2555
16. C. Delalondre, A. Douce, M. Gonzales, A. Gleizes, and J.-B. Guillot, 3D Fluid Dynamic Modelling of Electric Arcs, *Proc. 14th Int. Symp. Plasma Chem.*, 1999, **1**, p 321-326
17. M. Kelkar and J. Heberlein, Physics of an Arc in Cross Flow, *J. Phys. D: Appl. Phys.*, 2000, **33**, p 2172-2182
18. P. Freton, J.J. Gonzalez, and A. Gleizes, Comparison between a Two- and a Three-Dimensional Arc Plasma Configuration, *J. Phys. D: Appl. Phys.*, 2000, **33**, p 2442-2452
19. He-Ping Li and Xi Chen, Three-Dimensional Modelling of a DC Non-Transferred Arc Plasma Torch, *J. Phys. D: Appl. Phys.*, 2001, **34**, p L99-L102
20. He-Ping Li and Xi Chen, Three-Dimensional Modelling of the Flow and Heat Transfer in a Laminar Non-Transferred Arc Plasma Torch, *Chinese Phys.*, 2002, **11**(1), p 44-49
21. He-Ping Li, E. Pfender, and Xi Chen, Application of Steenbeck's Minimum Principle for Three-Dimensional Modeling of DC Arc Plasma Torches, *J. Phys. D: Appl. Phys.*, 2003, **36**, p 1084-1096
22. He-Ping Li, E. Pfender, and Xi Chen, Prediction of Anode Arc Root Position in a DC Arc Plasma Torch, *Proceedings of the 16th International Symposium on Plasma Chemistry*, Taormina, Italy, June 22-27, 2003
23. W. Finkelnburg, and H. Maecker, ''Electric Arcs and Thermal Plasmas,'' in *Encyclopedia of Physics*, Vol. XXII, Springer-Verlag, Berlin, 1956
24. C. Baudry, G. Mariaux, A. Vardelle, C. Delalondre, and E. Meillot, Modeling of Arc Formation in a DC Plasma Spray Torch, *Proceedings of the 16th International Symposium on Plasma Chemistry*, Taormina, Italy, June 22-27, 2003
25. G. Mariaux and A. Vardelle, 3-D Time-Dependent Modelling of the Plasma Spray Process, Part 1: Flow Modeling, *Int. J. Therm. Sci.*, 2005, **44**, p 357-366
26. Y.C. Lee, K.C. Hsu, and E. Pfender, Modeling of Particles Injected into a D.C. Plasma Jet, *Proceedings of the 5th International Symposium on Plasma Chemistry*, Heriot-Watt University, Edinburgh, Scotland, Vol. 2, 1981, p 795–803
27. J. McKelliget, J. Szekely, M. Vardelle, and P. Fauchais, Temperature and Velocity Fields in a Gas Stream Exiting a Plasma Torch. A Mathematical Model and Its Experimental Verification, *Plasma Chem. Plasma Process.*, 1982, **2**(3), p 317-332
28. Xi Chen, Y. C. Lee, and E. Pfender, The Importance of Knudsen and Evaporation Effects on Modelling in Thermal Plasma Processing, *Proc. 6th Int. Symp. Plasma Chem*. (July 1983, Montreal, Canada), Vol. 1, 1983, p 51–58
29. N. El-Kaddah, J. McKelliget, and J. Szekely, Heat Transfer and Fluid Flow in Plasma Spraying, *Metallur. Trans. B*, 1984, **15**, p 59-70
30. E. Pfender and Y.C. Lee, Particle Dynamics and Particle Heat and Mass Transfer in Thermal Plasma. Part I. The Motion of a Single Particle without Thermal Effects, *Plasma Chem. Plasma Process.*, 1985, **5**(3), p 211-225
31. Y.C. Lee, Y.P. Chyou, and E. Pfender, Particle Dynamics and Particle Heat and Mass transfer in Thermal Plasma. Part II. Partical Heat and Mass Transfer in Thermal Plasmas, *Plasma Chem. Plasma Process.*, 1985, **5**(4), p 391-414
32. Y.C. Lee and E. Pfender, Particle Dynamics and Particle Heat and Mass Transfer in Thermal Plasma. Part III. Thermal Plasma Jet Reactors and Multiparticle Injection, *Plasma Chem. Plasma Process.*, 1987, **7**(1), p 1-27
33. A.H. Dilawari and J. Szekely, Some Perspectives on the Modelling of Plasma Jets, *Plasma Chem. Plasma Process.*, 1987, **7**(3), p 317-329
34. Y.P. Chyou and E. Pfender, Behavior of Particulates in Thermal Plasma Flows, *Plasma Chem. Plasma Process.*, 1989, **9**(1), p 45-71
35. Y.P. Chyou and E. Pfender, Modeling of Plasma Jets with Superimposed Vortex Flow, *Plasma Chem. Plasma Process.*, 1989, **9**(2), p 291-328
36. R. Westhoff, G. Trapaga, and J. Szekely, Plasma-Particle Interactions in Plasma Spraying Systems, *Metallur. Trans. B*, 1992, **23**, p 683-693
37. J.D. Ramshaw and C.H. Chang, Computational Fluid Dynamics Modeling of Multicomponent Thermal Plasmas, *Plasma Chem. Plasma Process.*, 1992, **12**(3), p 299-325
38. C.H. Chang and J.D. Ramshaw, Numerical Simulations of Argon Plasma Jets Flowing into Cold Air, *Plasma Chem. Plasma Process.*, 1993, **13**(2), p 189-209
39. J.R. Fincke, C.H. Chang, W.D. Swank, and D.C. Haggard, Entrainment and Demixing in Subsonic Thermal Plasma Jets: Comparison of Measurements and Predictions, *Int. J. Heat Mass Trnasfer*, 1994, **37**(11), p 1673-1682
40. J.M. Bauchire, J.J. Gonzalez, and P. Proulx, Modelling of the Plasma-Particle Interactions in a Plasma Jet, *J. Phys. D: Appl. Phys.*, 1999, **32**, p 675-681
41. Y.P. Wan, V. Prasad, G.-X. Wang, S. Sampath, and J.R. Fincke, Model and Powder Particle Heating, Melting, Resolidification, and Evaporation in Plasma Spraying Processes, *ASME J. Heat Transfer*, 1999, **121**, p 691-699
42. R.L. Williamson, J.R. Fincke, and C.H. Chang, A Computational Examination of the Sources of Statistical Variance in Particle Parameters During Thermal Plasma Spraying, *Plasma Chem. Plasma Process.*, 2000, **20**(3), p 299-324
43. B. Liu, T. Zhang, and D.T. Gawne, Computational Analysis of the Influence of Process Parameters on the Flow Field of a Plasma Jet, *Surf. Coatings Technol.*, 2000, **132**, p 202-216
44. B. Dussoubs, A. Vardelle, M. Vardelle, P. Fauchais, and N.J. Themelis, *Proc. 13th Int. Symp. Plasma Chem*. (August 18-22, 1997, Beijing, China), Supplement, Peking University Press, 1997, p 2056–2061

45. B. Dussoubs, P. Fauchais, A. Vardelle, M. Vardelle, and N.J. Themelis, *Thermal Spray: A United Forum for Scientific and Technological Advances*, C.C. Berndt, Ed., ASM International, Materials Park, Ohio, USA, 1997, p 557
46. M. Leylavergne, B. Dussoubs, A. Vardelle, and N. Goubot, Comparison of Plasma-Sprayed Coatings Produced in Argon or Nitrogen Atmosphere, *J. Thermal Spray Technol.*, 1998, **7**(4), p 527-536
47. A. Vardelle, P. Fauchais, B. Dussoubs, and N.J. Themelis, Heat Generation and Particle Injection in a Thermal Plasma Torch, *Plasma Chem. Plasma Process.*, 1998, **18**(4), p 551-574
48. He-Ping Li and Xi Chen, Three-Dimensional Simulation of a Plasma Jet with Transverse Particle and Carrying Gas Injection, *Thin Solid Films*, 2001, **390**(1-2), p 175-180
49. He-Ping Li and Xi Chen, Three-Dimensional Modeling of the Turbulent Plasma Jet Impinging upon a Flat Plate and with Transverse Particle and Carrier-Gas Injection, *Plasma Chem. Plasma Process.*, 2002, **22**(1), p 27-58
50. Xi Chen and He-Ping Li, Three-Dimensional Flow and Heat Transfer in Thermal Plasma Systems, *Surf. Coat. Technol.*, 2003, **171**, p 124-133
51. K. Ramachandran and H. Nishiyama, Three-Dimensional Effects of Carrier Gas and Particle Injections on the Thermo-Fluid Fields of Plasma Jets, *J. Phys. D: Appl. Phys.*, 2002, **35**, p 307-317
52. K. Ramachandran, N. Kikukawa, and H. Nishiyama, 3D Modeling of Plasma–Particle Interactions in a Plasma Jet under Dense Loading Conditions, *Thin Solid Films*, 2003, **435**, p 298-306
53. Peng Han, Lan Yu, and Xi Chen, Modeling of Plasma Jets with Computed Inlet Profiles, *Proceedings of the 13th International Symposium on Plasma Chemistry* (August 18-22, 1997, Beijing, China), Peking University Press, Vol. 1, 1997, p 338-343
54. He-Ping Li, and Xi Chen, The Effects of the Joule Heating on the DC Arc Plasma Jet Characteristics, *Proceedings of the 16th International Symposium on Plasma Chemistry*, Taormina, Italy, June 22-27, 2003, Paper ISPC16-106
55. S.V. Patankar, *Numerical Heat Transfer and Fluid Flow*, Hemisphere Publishing, Taylor and Francis, 1980
56. J. Zhu, *An Introduction and Guide to the Computer Program FAST-3D*, Institute for Hydromechanics, University of Karlsruhe, Report No. 691, 1992
57. T. Zhang, D.T. Gawne, and B. Liu, Computer Modelling of the Influence of Process Parameters on the Heating and Acceleration of Particles during Plasma Spraying, *Surf. Coatings Technol.*, 2000, **132**, p 233-243
58. R. Ye, P. Proulx, and M.I. Boulos, Particle Turbulent Dispersion and Loading Effects in an Inductively Coupled Radio Frequency Plasma, *J. Phys. D: Appl. Phys.*, 2000, **33**, p 2154-2162